ChemPhysChem

Articles
doi.org/10.1002/cphc.202100709

Chemistry Europe
European Chemical Societies Publishing

www.chemphyschem.org

Comparative Hydrophobic Core Dynamics Between Wild-Type Amyloid-β Fibrils, Glutamate-3 Truncation, and Serine-8 Phosphorylation

Liliya Vugmeyster,*[a] Dan Fai Au,[a] Matthew C. Smith,[a] and Dmitry Ostrovsky[b]

Post-translational modifications (PTMs) of amyloid-β (Aβ) species are implicated in the modulation of overall toxicities and aggregation propensities. We investigated the internal dynamics in the hydrophobic core of the truncated ΔE3 mutant fibrils of $Aβ_{1–40}$ and compared them with prior and new data for wild-type fibrils as well as with phosphorylated S8 fibrils. Deuteron static solid-state NMR techniques, spanning line-shape analysis, longitudinal relaxation, and chemical exchange saturation transfer methods, were employed to assess the rotameric jumps of several methyl-bearing and aromatic groups in the core of the fibrils. Taken together, the results indicate the rather significant influence of the PTMs on the hydrophobic core dynamics, which propagates far beyond the local site of the chemical modification. The phosphorylated S8 fibrils display an overall rigidifying of the core based on the higher activation barriers of motions than the wild-type fibrils, whereas the ΔE3 fibrils induce a broader variety of changes, some of which are thermodynamic in nature rather than the kinetic ones.

1. Introduction

Fibrils and oligomers of amyloid-β (Aβ) protein are implicated as hallmarks of Alzheimer's disease.[1] The accumulation of toxic Aβ species can be a trigger of the cascade of pathological steps involving, among other proteins, tau and α-syneclein.[2–3] The range of pathological species is very broad and challenging to define. Rasmussen et al. found that polymorphic Aβ deposits within the brain cluster as clouds of conformational variants in different Alzheimer's disease cases.[4–6] Post-translational modifications (PTMs) of Aβ have been increasingly brought to attention as toxicity modulators.[2,7,8] Yet, structural and dynamics studies of PTMs are relatively sparse. Many PTMs occur in the disordered N-terminal region (residues 1–16).[8] Of relevance to this work are the phosphorylation of serine-8 (pS8) and truncation of the peptide at the glutamate-3 position (ΔE3).

pS8-type fibrils are implicated in late-onset Alzheimer's.[9–11] From a structural perspective, they are similar to the wild-type striated-ribbon 2-fold morphology structure (wt-2f)[12–13] with the in-register parallel β-sheet.[14] pS8 fibrils have been found to have increased nucleation-dependent fibrillation and enhanced Aβ-mediated toxicity.[14–16] We have recently shown that the internal dynamics of both the N-terminal and the C-terminal domains are more rigid than those of the wild-type protein, as probed by deuterium solid-state NMR studies.[6,14] The structure of the N-terminal domain is more pronounced in intra-strand contacts than the wild-type structure and the hydrophobic core appears to be tighter.[14]

ΔE3 truncation is one example of when shortening the sequence may lead to higher aggregation propensities.[8,17–18] This truncation also initiates the generation of the pyroglutamate-3 modification, which has been shown to be aggressive in promoting aggregation.[8] Fibrillation kinetics and morphologies, as assessed by transmission electron microscopy, have been found to be similar between the ΔE3 truncation and pyroglutamate-3 modifications, showing more rapid nucleation-dependent fibrillation and fragmented fibrils morphology in both cases.[15,19] Solid-state NMR analysis of chemical shifts points toward high similarity between the secondary structure and key tertiary contacts of the wild-type and pyroglutamate-3 fibrils structures.[20] Additionally, a recent work by Hu et al.[21] detected several structural differences between the wild-type fibrils and the ΔE3 or pyroglutamate-3 fibrils: in the modified fibrils, the core with parallel β-sheet structure extended further toward the N-terminal domain into the G9 to V12 region, based on circular dichroism measurements as well a ^{13}C solid-state NMR distance measurements for selected sites. Our studies of the dynamics have suggested that the N-terminal domain dynamics are somewhat more enhanced at the residue G9 compared to the wild-type protein,[6] in line with the morphological fragmentation but perhaps not immediately intuitive if the structure comprises a regular parallel β-sheet all the way up to G9 site.

The dynamics of the hydrophobic core of the C-terminal domain have not previously been assessed for the ΔE3 modification. In this work, we compare the intrinsic flexibility of the C-terminal domain hydrophobic core in the wt-2f, pS8, and ΔE3 fibrils. All the fibrils are grown with similar seeded growth protocols. Dynamics studies complement the structural investigations to define the complete conformational ensembles that

[a] Dr. L. Vugmeyster, D. Fai Au, M. C. Smith
Department of Chemistry,
University of Colorado Denver
Denver, CO, 80204, USA
E-mail: liliya.vugmeyster@ucdenver.edu
[b] Dr. D. Ostrovsky
Department of Mathematics,
University of Colorado Denver
Denver, CO, 80204, USA

Supporting information for this article is available on the WWW under https://doi.org/10.1002/cphc.202100709

encompass the different unique sub-states that could drive aggregation propensities.

The deuterium solid-state NMR techniques used in this work are well suited for the investigation of the dynamics of non-crystalline aggregates and fibrils.[22–23] Under static conditions, they require the introduction of site-specific labels and thus we work with synthetic peptides that incorporate deuterium labels at selected hydrophobic core positions. We use static line-shape analysis and recently developed deuteron chemical exchange saturation transfer (CEST) measurements[24] to assess the rotameric motions in the methyl-bearing side-chains of L17, L34, M35, and V36 residues as well as longitudinal relaxation to assess the ring-flipping motion of the F19 side-chain (Figure 1A). Line-shape and relaxation measurement data for the pS8 and wild-type fibrils are taken from previous work.[14,25] As we show, both PTMs lead to changes in hydrophobic core flexibility, with pS8 clearly rigidifying the core, while ΔE3 displays a more diverse set of changes, some of which are thermodynamic rather than kinetic in origin.

2. Results and Discussion

2.1. Details of the Systems Investigated

Figure 1A shows the key hydrophobic core side-chains probed in this work. With the exception of the aromatic F19 side-chain, all the other side-chains are methyl-bearing. The top view of a single unit of the fibrils is shown as a ribbon diagram for the wt 2-fold symmetric $A\beta_{1-40}$ structure.[12–13] pS8 fibrils form a similar quaternary structure,[14] while no structure is available for the ΔE3 fibrils. All the side-chains in these two known structures point directly into the hydrophobic core, with the exception of the M35 side-chain, which is oriented along the interface between the two symmetric sub-units. The exact positions of the hydrophobic core side-chains are not known for the ΔE3 variant. Fibril samples were prepared using established seeded-growth protocols and their morphologies confirmed with transmission electron microscopy(TEM), with representative images shown in Figure 1B. Only the ΔE3 samples were newly generated for this work, while the wt and pS8 fibrils were taken from prior studies.[14,25] The fibrils were hydrated with deuterium depleted water to about 200% content. The overall structures are believed to be very similar in the dry and wet states of the wild-type fibrils based on the chemical shifts measured with magic-angle spinning solid-state NMR.[12] However for several sites in the core (F19 and M35), as well as for all N-terminal domain sites, the dynamics was found to be significantly more pronounced in the presence of solvation.[25–28] We have also confirmed that lyophilization and hydration leaves the morphology intact, and the representative TEM images for the ΔE3 fibrils are shown in Figure S1 in the Supporting Information.

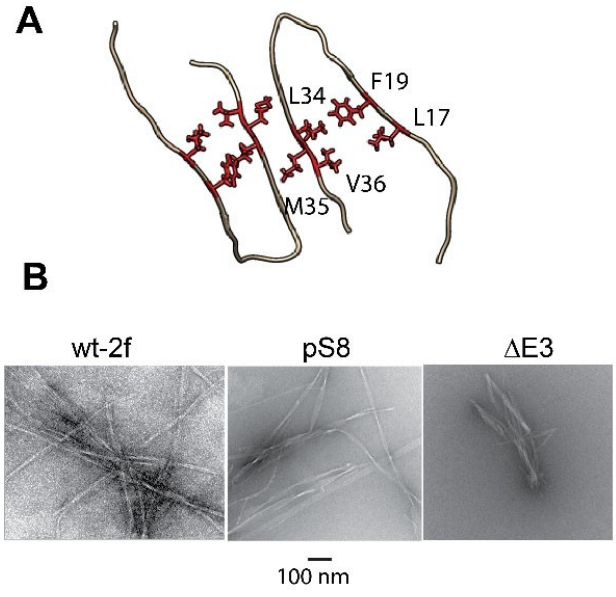

Figure 1. A) A ribbon diagram of the 2-fold symmetric wild-type $A\beta_{1-40}$ quaternary structure (view from the top) with the side-chains of L17, F19, L34, M35, and V36 investigated in this work shown in red. The structure corresponds to the pdb ID 2LMN. B) Negatively stained transmission electron microscopy images of $A\beta_{1-40}$ fibrils comprising the wild-type peptide and in the 2-fold symmetric polymorph (left), with the pS8 modification (center) and with the ΔE3 modification (right).

For the single-site labeling employed in the static ^2H solid-state NMR measurements, synthetic $A\beta_{1-40}$ peptides were generated containing selected deuterated amino acids. The labeling patterns are $-^{\delta}CD_3$ for L17 and L34, $-S-CD_3$ for M35, $-^{\beta}CD_2-(^{\gamma}CD_3)_2$ for V36, and $-^{\beta}CH_2-ring-D_5$ for F19. While leucine and methionine have labels at a single methyl group, all the aliphatic protons are replaced by deuterons in commercially available fluorenylmethoxycarbonyl-valine (with the protection group necessary for the incorporation into the peptide via solid-state peptide synthesis). Under the conditions of our studies, neither C^{α}/C^{β} nor deuterons contribute to the NMR signals.[29] While the phenylalanine ring of F19 has deuterons in all five positions, only the meta and otho deuterons contribute to the ring-flipping motions.

2.2. ^2H NMR Line-shape Analysis over a Broad Temperature Range of the Methyl-bearing Side-Chain for Assessing Rotameric Motions

Deuterium line shapes in the solid state can probe motions in the μs to ms range, whose time scales are comparable in magnitude to the quadrupolar coupling constant (C_q). For methyl groups, typical C_q values are in the 155 to 175 kHz range. Fast 3-site methyl jumps introduce an effective averaging by a factor of 1/3. The rotameric jumps of the side-chains (detailed in Figure 2) that occur on the slow time scale lead to distortions and narrow the line shapes in comparison to the rigid pattern. Observations of these changes as a function of temperature provide a means of determining the energy differences between the rotameric states and activation energies of the rotameric jumps. These parameters, in turn, reflect the packing and flexibility features of the hydrophobic core of the fibrils.

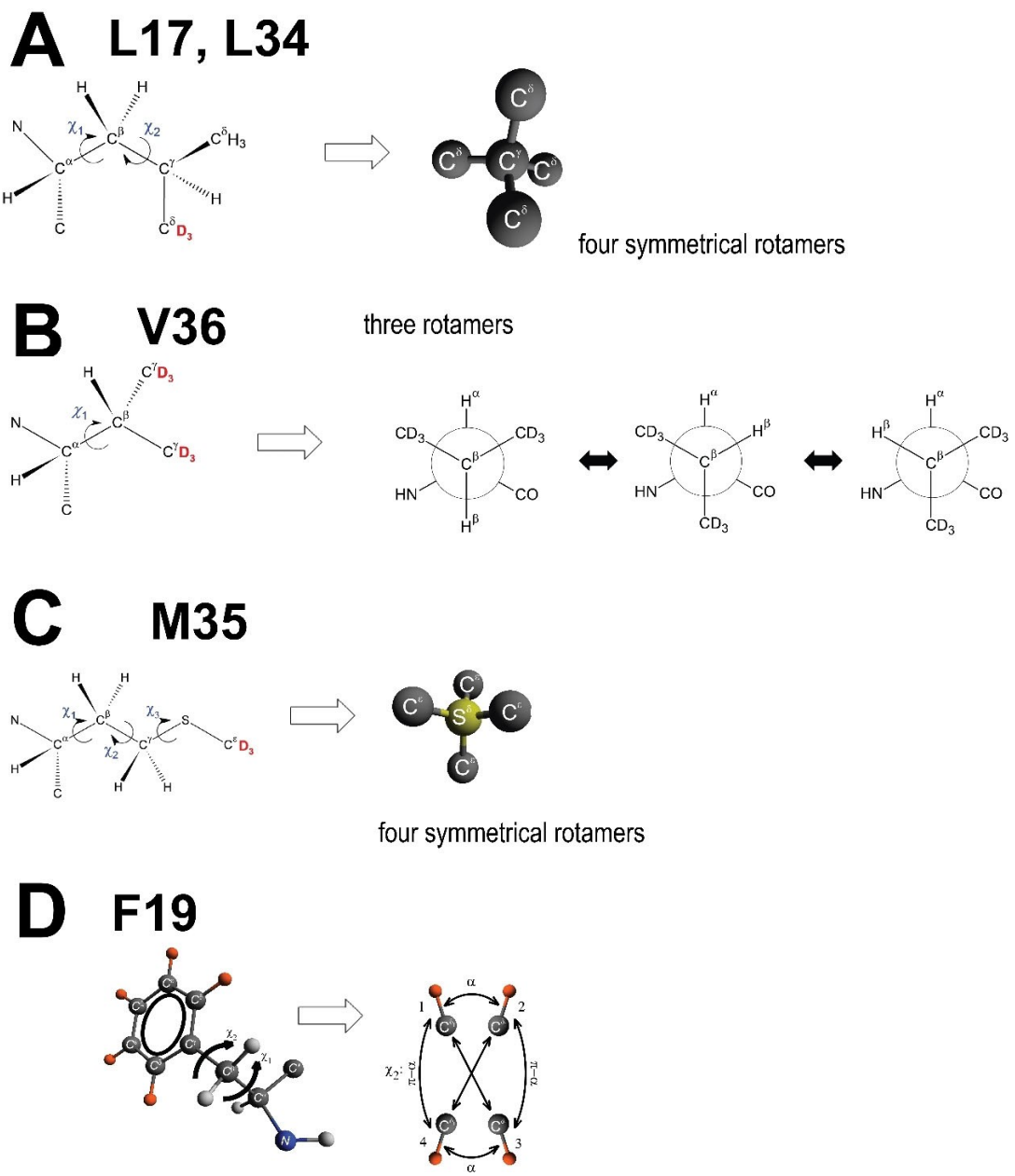

Figure 2. Motional models of A) L17, L34: Rotameric jumps around the χ_1 and χ_2 angles are represented by four magnetically non-equivalent conformers (out of the nine possible configurations) pointing toward the corners of a tetrahedron. The positions of the ^{2}H labels at the methyl groups of the side-chains are shown in red. B) V36: Rotameric jumps around the χ_1 angle are represented by three conformers, g^+, t, and g^-. C) M35: Rotameric jumps (involving in reality all three χ_1, χ_2, and χ_3 angles) are approximated by four artificial symmetrical conformers. D) F19: Aromatic ring-flips and small-angle fluctuations around the χ_2 dihedral angle in the phenylalanine side-chains. Left panel: The phenylalanine side-chain with the deuteron-labeling pattern marked in orange. The diagram to the right displays the sites' connectivities according to the 4-site strong collision model, illustrated for one of the C^δ–D bonds. The large-angle aromatic flips occur between sites 1–3 and 1–4 with an equal probability; this also holds for the 2–3 and 2–4 pairs. The small-angle jumps with the amplitude $\alpha = 5°$ occur between sites 1–2 and 3–4.

The line shapes, using the quadrupolar echo detection scheme,[30] were collected for the hydrated ΔE3 fibrils over temperature ranges similar to those used for the wt-2f and pS8 fibrils, with representative results shown in Figure 3. Prior line shape data are shown in Figure S2 for completeness. The selected temperature ranges are governed by the steepness of the temperature dependence, with the exception of the M35 side-chains, as discussed below.

The simulated line shapes fitted to the data were parametrized according to previously developed rotameric models, as depicted in detail in Figure 2. For the valine side-chain, there is one degree of rotameric angle freedom (χ_1) with three rotamers in the standard g^+, t, and g^- conformations. For the leucine side-chain, there are two rotameric degrees of freedom (χ_1, χ_2), leading in principle to nine possible conformations. Studies have shown that they can be approximated by four

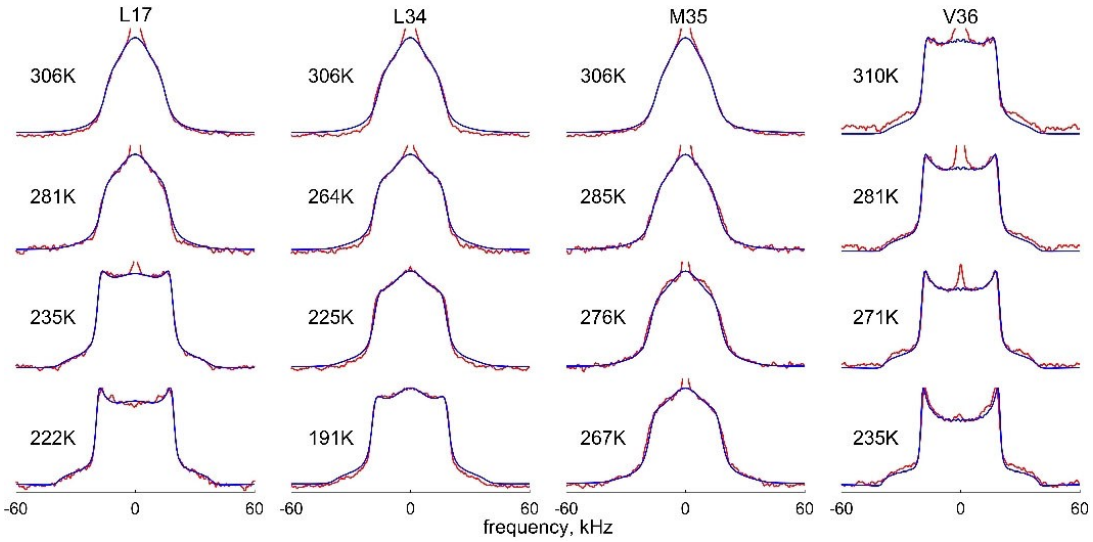

Figure 3. Typical ^{2}H static solid-state NMR line-shape analysis spectra for the hydrated ΔE3 Aβ fibrils, collected at 9.4 T using the quadrupolar echo scheme. Normalized experimental (red) and fitted (blue) spectra at several temperatures with the fits performed according to the models in Figure 2. The narrow peak at zero frequency is due to residual HOD signals.

symmetrical conformers pointing to the corners of the tetrahedron within experimental precision.[31] For methionine, which has the longest side-chain and three side-chain dihedral angles (χ_1, χ_2, χ_3), the situation is the most complex. Based on previous studies,[25] at temperatures below about 250 K at which the hydration layer is largely frozen, it is sufficient to model the dynamics with three conformers. This scenario may indicate that only the χ_3 interconversions are active. However, at higher temperatures, the onset of solvent-dependent changes requires the introduction of additional rotameric states. Similar to the approach for leucine side-chains, we model the rotameric states of the M35 side-chains at high temperatures using four symmetrical artificial conformers with tetrahedral geometry.

For all the cases of line-shape data modeling, it was sufficient to introduce one major rotamer (i.e., w:1:1 population ratios for the valine side-chain and w:1:1:1 for the leucine and methionine side-chains for which four symmetrical rotamers are employed; $w > 1$ stands for the relative weight of a single major conformer) and one single rotameric exchange constant k_{rot} between all the rotameric states. The temperature dependence of k_{rot} is assumed to be Arrhenius and it yields the activation energy E_a of the rotameric motions (Figures 4 and 5).

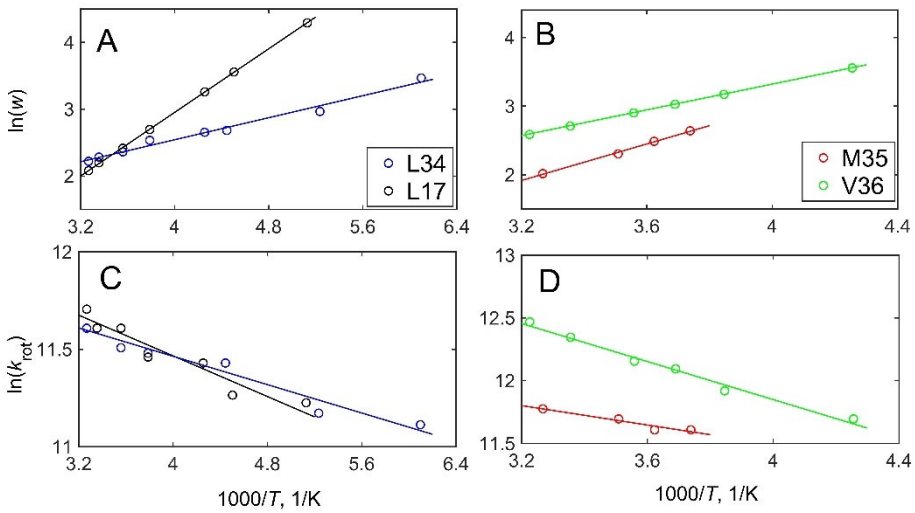

Figure 4. Modeled parameters fits for the ΔE3 Aβ fibrils. A,B) rotameric populations, ln(w) vs 1000/T (A,B), obtained from the line-shape data of Figure 3 and using the model of a single major rotameter (w:1:1 model for V36, w:1:1:1 model for L17, L34, and M35, see Figure 1) as well as the rotameric exchange rates, ln(k_{rot}) vs 1000/T (C,D). Circles represent the fitted values to the line-shape data at individual temperatures; solid lines demonstrate global fits at all temperatures as outlined in the text.

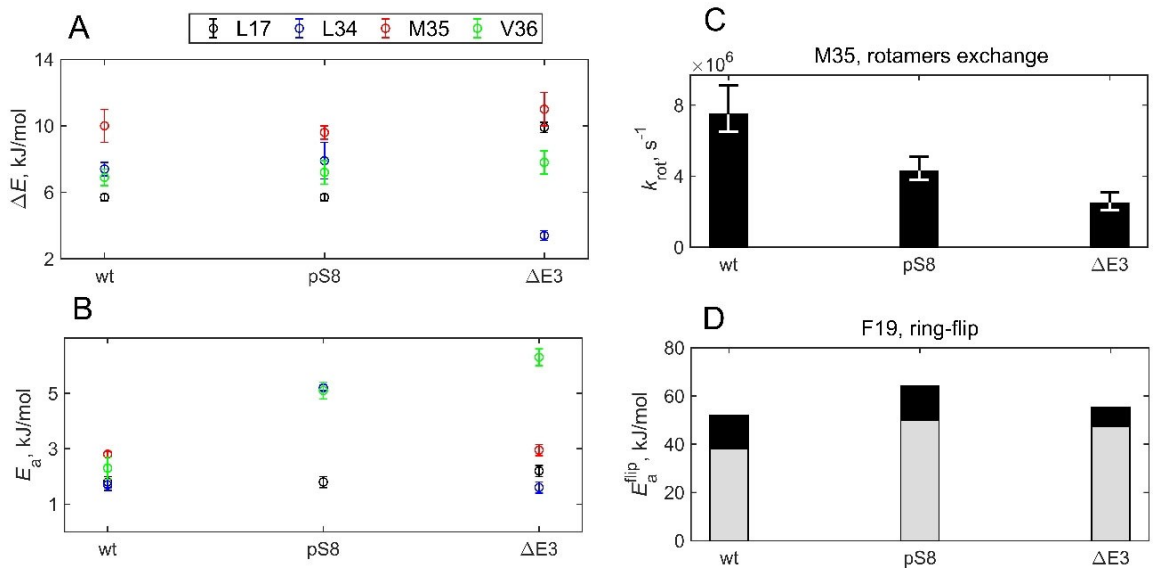

Figure 5. Comparison of the fitted modeled parameters for all the hydrophobic core side-chains probed in the wt-2f, pS8, and ΔE3 hydrated $A\beta_{1-40}$ fibrils. A) ΔE energy difference between the major and minor rotamers in the L17, L34, M35, and V36 side-chains, assuming a single major rotameric state. B) Activation energies E_a of the rotameric jumps in the L17, L34, M35, and V36 side-chains. C) Rotameric exchange rate constant k_{rot} at 37 °C for the M35 side-chains obtained on the basis of the ^{2}H CEST measurements, modeled by two major and two minor rotamers in the 6:6:1:1 ratio for all the variants. D) Activation energies E_a^{flip} for the F19-ring-D5 aromatic ring-flipping motion. The black bars show the ranges from $\langle E_a^{flip}\rangle - \sigma^{flip}$ to $\langle E_a^{flip}\rangle + \sigma^{flip}$.

The temperature dependence of w follows a Boltzmann-type equation with a non-zero intercept, yielding as one of the parameters ΔE, which is the energy difference between the major and minor rotameric states (Figures 4 and 5). The modeling was performed according to previously developed procedures.[25,31–32] All of the parameters are defined in Table 1.

For the M35 side-chain, the ΔE3 line shapes at low temperatures below about 250 K are similar for all types of fibrils probed and lead to the same values of E_a (1.7–1.8 kJ/mol) and ΔE (8.5 kJ/mol) within the experimental precision. The data and details of the analysis are shown in Figure S3. This suggests that unfreezing the hydration layer is important for creating the unique packing differences between the symmetrical subunits of the fibrils. Thus, for the M35 site, we focus on quantification of the parameters at temperatures above 250 K, at which the effects of hydration activate additional rotameric states, as modeled in Figure 2C. M35 points toward the interface between the two symmetrical units of the 2-fold structure (Figure 1) and the 3-fold symmetric wild-type structure defines the contacts in the water accessible cavity.[28,33–34]

The E_a values are similar for the ΔE3 fibrils at the L17, L34, and M35 sites in comparison to the wt-2f fibrils (1.6–2.95 kJ/mol range), but significantly higher at the V36 site: 6.3 ± 0.3 kJ/mol for the ΔE3 variant in comparison to 2.3 ± 0.4 kJ/mol for the wt-2f fibrils. For the pS8 fibrils, the activation energy barriers were significantly larger for all but the L17 side-chain. By contrast, while for the pS8 fibrils' the ΔE values were similar to those in the wt-2f fibrils, for the ΔE3 fibrils, the L17 and L34 side-chains have significantly different ΔE values (L34 in ΔE3: 3.4 ± 0.3 kJ/mol, in wt-2f: 7.4 ± 0.4 kJ/mol; L17 in ΔE3: 9.9 ± 0.3 kJ/mol, in wt-2f: 5.7 ± 0.2 kJ/mol). The ΔE values for the M35 and V36 side-chains in the ΔE3 fibrils remain similar to those in the wt-2f fibrils. Thus, the ΔE3 PTM induces several changes in the internal dynamics via thermodynamics effects rather than kinetic ones based on the line-shape measurements. Additionally, the higher activation energy barrier for V36 indicates that the core is tightened at its C-terminal end.

Table 1. Definitions of the modeled parameters.

Parameter	Definition
w	Occupation number of the dominant rotameric state relative to the minor states
k_{rot}	Exchange rate between any two rotameric states defined as a sum of the forward and backward rates
E_a	Activation energy of rotameric exchange, $k_{rot} = k_0 e^{-E_a/RT}$
ΔE	Energy difference between the major and minor rotameric states used in the Boltzmann relation, $w = e^{b/R-\Delta E/RT}$
T_1^{eff} and β	Fitting parameters of magnetization decay curves according to the stretched exponential function: $M(t) - M(\infty) = (M(0) - M(\infty))e^{-(t/T_1^{eff})^{\beta}}$
k_{flip}	Flip (exchange) rate between the two orientations of phenylalanine ring (i.e., π-flip)
$\langle E_a^{flip}\rangle$	Average activation energy for π-flips of a phenylalanine ring
σ^{flip}	Standard deviation of the Gaussian distribution of activation energy for π-flips of a phenylalanine ring
$\langle E_a^{small}\rangle$	Average activation energy for small-angle fluctuations around the χ_2 dihedral angle in a phenylalanine ring, with the amplitude of $\alpha/2 = 5°$
σ^{small}	Standard deviation of the Gaussian distribution of activation energy for the small-angle fluctuations of a phenylalanine ring

2.3. Quadrupolar CEST Measurements at the M35 Side-Chain for Detailed Rotameric Interconversion Evaluation

Because of the importance of the M35 side-chain in the characterization of the inter-unit contacts, we also probed its dynamics using a more sophisticated ^{2}H NMR technique that is especially sensitive to slower time scale motions. ^{2}H NMR CEST measurements[24] use low power saturation applied as a function of the off-resonance offset for the precise determination of conformational exchange processes. We have recently applied this technique for the M35 side-chain in the 3-fold symmetric polymorph,[24,35] which revealed that the rotameric exchange is more complex than that seen by the line shapes alone. In particular, this measurement indicated the presence of at least two major conformational states within the 4-state rotameric model in Figure 2C. In this work, we probed the M35 side-chains in the wt-2f, pS8, and ΔE3 fibrils using ^{2}H CEST measurements under static conditions at 37 °C.

The resulting saturation profiles (i.e. the signal intensity integrated over the −10 to 10 kHz spectral region versus the off-resonance offset) are shown in Figure 6. A saturation field strength of 1.3 kHz and saturation time of 20 ms were chosen based on previous optimizations.[24] The longitudinal relaxation times are of the order of 300 ms and do not compete significantly with the conformational exchange processes in modulating the signal intensity. As in the case of the 3-fold symmetric polymorph, it was found that parametrization with a single major rotamer with a population ratio of w:1:1:1 cannot reconcile both the line-shape and the CEST results. It is thus necessary to use the model of two major conformers in the w:w:1:1 ratio with a single k_{rot} rate constant. As a first approximation, it was sufficient to constrain the value of $w=6$ for all the variants in order not to overfit the data at the single temperature, as the fitted values of k_{rot} and w may be correlated. The resulting fitted values of k_{rot} are shown in Figure 5C. In comparison with the wt-2f fibrils ($k_{rot}=7.5\cdot10^6$ s^{-1}), the values in the pS8 and ΔE3 fibrils fall to $k_{rot}=2.2\cdot10^6$ s^{-1} and $k_{rot}=2.8\cdot10^6$ s^{-1}, respectively (Figure 5C). An example of the quality of the fit is shown in Figure S4 for the wt-2f fibrils. There is weak dependence of the fitted value of k_{rot} on the chosen value of w. Overall, the results imply a restriction/slowing of the rotameric exchange at the physiological temperatures in the PTMs, which is somewhat more pronounced for the pS8 fibrils.

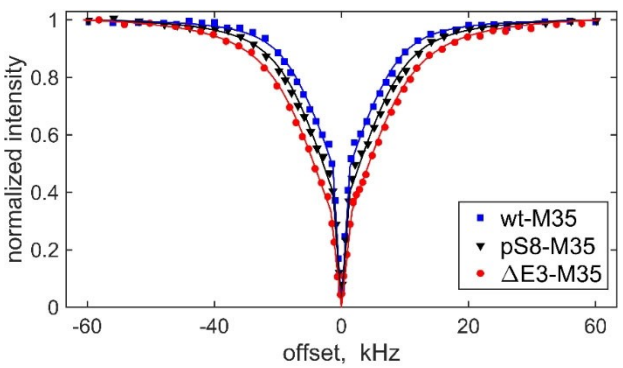

Figure 6. Normalized ^{2}H CEST intensities (integrated over the −10 to 10 kHz spectral region) versus the off-resonance offsets for the M35 side-chains in the wt Aβ_{1-40} fibrils in the 2-fold symmetric polymorph and in the pS8 and ΔE3 variants. The measurements have been performed at 9.4 T under static conditions and at 37 °C. The saturation field strength was 1.3 kHz and the saturation time was 20 ms. The lines represent the fits to the rotameric exchange model of the four symmetrical conformers (Figure 2C) with two major and two minor states in the population ratio of 6:6:1:1.

2.4. ^{2}H Longitudinal Relaxation for Assessing the Ring-flipping Motion of F19

The aromatic ring-flips of the F19 side-chain, which points inside the hydrophobic core at least in the wild-type and the pS8 fibrils, stand out from the methyl probes: they have the potential to sense a different subset of motions in the core, including concerted rearrangements.[27,36–38] While line-shape measurements can probe aromatic ring-flips at higher temperatures, at around 270 K the powder pattern become rigid-like and longitudinal relaxation measurements are more suitable for the determination of the activation energies of the ring-flipping motions in the fibrils.[38–39] Based on previous results, the dynamics of the F19 side-chain are complex, with ring-flipping motions driving the relaxation at temperatures above 260 K and small-angle fluctuations dominant at lower temperatures (Figure 2D).[27] As for the pS8 fibrils,[14] we assumed that the small-angle fluctuations are the same in all the types of fibrils due to their dependence mostly on local structural factors. We, thus, only probed directly the large-angle motions, fixing the parameters of the small-angle fluctuations around the χ_2 angle at the values found for the wt-2f fibrils, listed explicitly in the Experimental section.

To enhance the signal, the multiple echo acquisition scheme was employed,[40] which breaks the powder pattern into a series of spikes, in our case separated by 16 kHz (Figure 7A). The magnetization decay or build-up curves $M(t)$ can then be recorded at the chosen spikelet locations, as the anisotropy is retained in this technique.[41] We focus on the ±16 and ±64 kHz positions (Figure 7B).

In general, relaxation is non-exponential, reflecting the heterogeneity of core packing. The decay curves are fitted by the stretch-exponential function of the form $M(t)-M(\infty)=(M(0)-M(\infty))e^{-(t/T_1^{eff})^{\beta}}$, in which $M(t)$ is the signal intensity, T_1^{eff} is the effective relaxation time, and β is the parameter that reflects the degree of non-exponentiality, defined in the range of $0<\beta\leq1$. β less than 1 corresponds to non-exponential behavior. For the saturation recovery measurements, $M(t)=0$. The values of T_1^{eff} and β for all the temperatures (Figures 7C and 7D) are fitted to the global model in Figure 2D, which assumes an energy landscape with a Gaussian distribution of activation energies for the ring-flips. The main fitting parameters are $\langle E_a^{flip}\rangle$ as the central value and σ^{flip} as the width of the distribution, assuming that the individual rate constants with the ensemble follow Arrhenius temperature dependence. Prior results on the wt-2f and pS8 fibrils are included in Figure S5 for completeness. Additionally, in Fig-

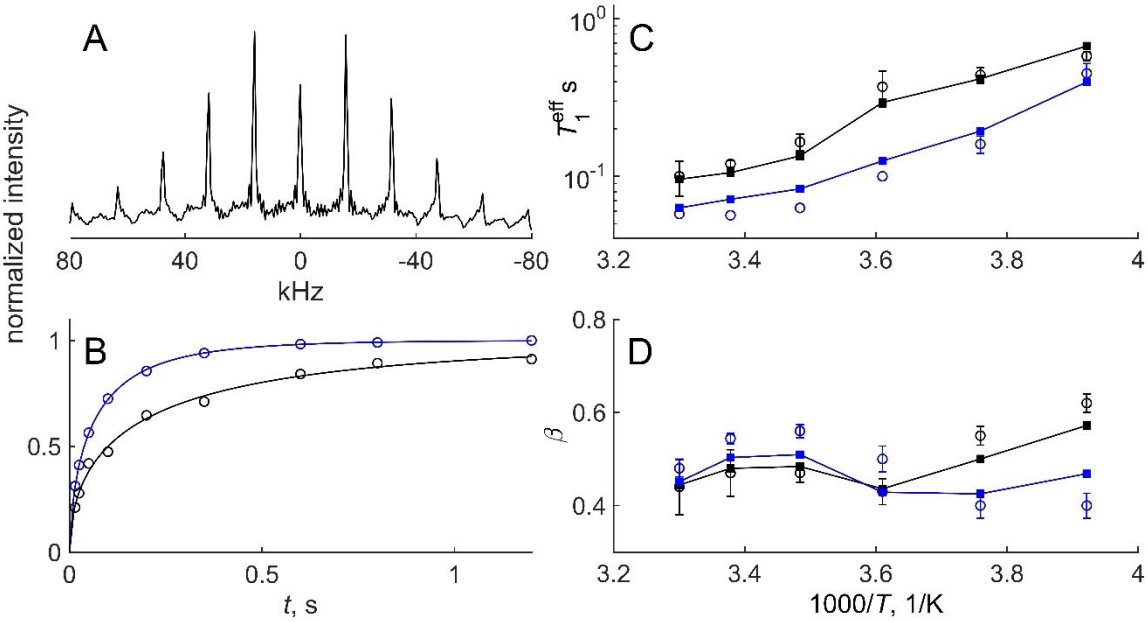

Figure 7. ^{2}H static NMR longitudinal relaxation measurement data for the F19-ring-D5 site in the ΔE3 Aβ fibrils, collected at 9.4 T. A) Examples of the spectra collected with the multiple-echo acquisition scheme, shown for 280 K, demonstrating the spikelet pattern spaced at 16 kHz intervals. B) Normalized magnetization build-up curves for the spikelets at ±16 kHz (blue) and ±64 kHz (black) at 280 K, resulting from the saturation recovery measurements. The lines represent the fits to the stretched exponential function. C,D) Resulting values of T_1^{eff} and β versus 1000/*T*. The joint fit of the experimental data at the ±16 kHz and ±64 kHz spikelets was performed at each individual temperature with the model of the log-normal distributions of the aromatic ring-flip rate constant k_{flip}, detailed in the text (filled squares connected by lines to guide the eye). Error bars smaller than the sizes of the symbols are not shown.

ure S6 we show the details of the global fit for the ΔE3 fibrils over the entire temperature range.

Figure 5D compares the resulting values of $\langle E_a^{flip} \rangle$ and σ^{flip} for all the variants. Both the pS8 and the ΔE3 fibrils display increased $\langle E_a^{flip} \rangle$ values: 45±3, 57±3, and 51±3 kJ/mol for the wt-2f, pS8, and ΔE3 variants, respectively. The widths of the distributions are comparable in the wt-2f and pS8 fibrils (around 7 kJ/mol), while the σ^{flip} of 4 kJ/mol is significantly smaller in the ΔE3 fibrils. Thus, both PTMs lead to an overall tightening of the aromatic ring environment in the core, with a significantly narrow range of activation energies for the ΔE3 fibrils.

Based on all of the results, the global picture of the effect of PTMs indicate that the intrinsic flexibility of the fibrils is clearly affected by the PTMs. These modifications reduce the flexibility at the F19 aromatic side-chain and the M35 side-chain, the latter pointing toward the interface between the symmetrical subunits in the wild-type structure. For the methyl-bearing side-chains pointing directly into the core in the wild-type structure, the situation is more complex. The L17 and L34 sites experience changes in the rotameric populations for the ΔE3 variant rather than changes in activation energy, which were seen for the pS8 variant, pointing at the thermodynamic factors in play rather than the kinetic ones in driving the differences. The activation energy at the V36 site is significantly higher in the ΔE3 fibrils. As emphasized above, the exact positions of the side-chains for the ΔE3 variants are not yet known.

In general, the results suggest the rather significant influence of PTMs on hydrophobic core dynamics in addition to the previously identified effect on the dynamics of the disordered N-terminal domain.[6] Thus, while the chemical modifications probed here are located in the N-terminal region, their effects on the dynamics propagate well into the core and are not confined to the local regions of the change. PTMs can be responsible for aggressive aggregation-prone states that have the potential to propagate into the more abundant wild-type fibrils upon cross-seeding,[8,15–16] i.e., very low concentration of the PTMs inducing its structural and aggregation propensities for the abundant wild-type Aβ fibrils.[42] Hu at el. demonstrated that cross-seeded wild-type fibrils retain some features of the PTMs structure for the ΔE3 modification.[21]

It is expected that at least some of the differences in intrinsic flexibility can propagate into the cross-seeded fibrils as well. It remains to be seen in future studies whether this is indeed the case. Additionally, the structures of the ΔE3 fibrils as well as that of the downstream pyro-glutamate variant will further enhance our understanding of the alternations in the conformational ensembles in the presence of the PTMs.

3. Conclusions

The dynamics in the hydrophobic core of the fibrils, spanning the ordered C-terminal domain, are clearly sensitive to the chemical nature of the PTMs. These changes in the dynamics propagate well beyond the local sites of the structural modifications, which in our case are located in the disordered N-terminal domain. While the pS8 modification induces overall rigidity, as deduced from the higher activation energies of the

motions in the core in comparison to the wild-type fibrils, the ΔE3 truncation leads to more variable effects. At several sites, the activation energy barriers in the ΔE3 fibrils are higher than the wt-2f fibrils. This includes the F19 ring-flips, which are likely sensing the concerted fluctuations of the entire core. Interestingly, the width of the distribution of the activation energies for the ring-flipping motion is significantly reduced in the ΔE3 variant in comparison with both the wt-2f and the pS8 fibrils. The V36 site, located at the end of the core, displays a significantly higher activation energy barrier for the rotameric jumps, indicating that the core is tighter in the ΔE3 variant, similar to the pS8 fibrils. By contrast, for the L17 and L34 side-chains, the rotameric jumps retain similar activation energies to the wt-2f fibrils, but the populations of the rotameric states are rearranged, suggesting the underlying thermodynamic effects rather than kinetics. At the M35 site, which points toward the interface between the two symmetric sub-units, the rotameric exchange rate constant at the physiological temperature is increased in both PTMs in comparison to the wild-type fibrils based on the ^{2}H CEST results, while the line-shape analysis did not detect any differences between the wild-type fibrils and ΔE3 modification. In general, a suite of ^{2}H solid-state NMR techniques with sensitivity ranges to different time scales and amplitudes of motions was instrumental to delineate these differences, and this underscores the need to employ several techniques to compare the intrinsic flexibilities accurately.

In the context of the heterogeneity of Aβ fibrils' chemical structures and structural polymorphisms, several PTMs can cause enhanced aggregation properties in cross-seeding events. The aggregation-driving states, in general, can be relatively minor species within the entire conformational ensemble. Thus, while it is clearly important to obtain global structural information, the characterization of relatively minor populated states and their interconversions within the ensembles is essential to capture the global picture of the comparisons between the variants.

Experimental Section

Preparation of the ΔE3 Fibril Samples

Peptide synthesis: The peptides were prepared using solid-state peptide synthesis (Life Technologies Corporation, Carlsbad CA). The amino acids were purchased from Cambridge Isotopes laboratories (Andover, MA) and CDN isotopes (Pointe-Claire, Canada). The ΔE3 variant sequence was EFRHDSGYEVHHQKLVFFAEDVGSNK-GAIIGLMVGGVV. The peptides were purified by reversed-phase HPLC to the minimal purity level of 95% and their identity and purity were confirmed by mass spectrometry and reversed-phase HPLC (Figure S7).

Preparation of the ΔE3 fibril samples: Fibrils were grown following previous generation seeding protocols,[5–6] with the labeled fibrils corresponding to the generation number 5. Briefly, seeded generation growth used a 1:10 molar ratio of seeds, and this was achieved by incubation with gentle 40 rpm orbital agitation for 3–5 days at room temperature at a 0.5 mg/mL peptide concentration in 10 mM of monosodium phosphate buffer (pH 7.4, 0.05% NaN_3). The bulk fibrils for the NMR analysis were collected by centrifugal dialysis using Amicon filters with 3 kDa molecular weight cut-off. Collected fibrils were re-suspended in deionized water, rapidly frozen with liquid nitrogen, and lyophilized. The samples were packed in 5 mm NMR tubes (cut to 21 mm length) using Teflon tape to center the sample volume in the coil of the NMR probe. A hydrated state with a water content of 200% by weight was achieved by pipetting deuterium-depleted H_2O directly in the NMR tubes, followed by flash freezing the hydrated fibrils in the tubes in liquid nitrogen, defrosting, and equilibrating for at least 48 hours to ensure homogeneous hydration. Preparation of pS8 fibrils in prior work[14] followed the same procedure with the exception of the fibrils' collection step, which employed pelleting at 300,000 *g* for 7–9 hours. Preparation protocols of the wild-type fibrils in the 2-fold symmetric polymorph are listed in details in Petkova et al.[12] and Vugmeyster et al.[25]

Negatively Stained Transmission Electron Microscopy

Samples were stored at room temperature and diluted to about 0.1 mg/mL with hydro, millipore-filtered water. Samples were negatively stained using the drop method[43] in the following manner. Four microliter aliquots of the sample, millipore-filtered water, and 2% uranyl acetate aqueous stain were applied sequentially to a freshly glow-discharged,[44] Formvar carbon-coated 300 mesh copper grid for the following incubation times: 2 min, 10 sec, and 2 min, respectively. Each 4 μl droplet was removed by wicking with filter paper for 5 sec. The filter paper was blotted before the addition of the next droplet. After staining, the grid was air-dried under a vacuum for 20 min. Images were collected under low dose conditions of 120,000 magnification using an FEI Tecnai G2 Spirit Biotwin microscope operating at 80 kV.

NMR Procedures

Line-shape experiments for the ΔE3 fibrils labeled at one of the L17, L34, M35, and V36 side-chains were performed using a 9.4 T NMR spectrometer equipped with a static Phoenix probe with a 5 mm diameter coil. The quadrupole echo pulse sequence based on an eight-step phase cycle[45] was used, with a delay of 31 μs between 90° pulses. The duration of the 90° pulses was 2.0 μs. The number of scans varied from 2×1024 to 40×1024 depending on the signal-to-noise ratios. Higher temperatures required more scans. Relaxation delays were set to three times the longitudinal relaxation rates of the methyl deuterons, which were determined by either inversion recovery (for the leucine and valine residues) or saturation recovery (for the methionine residues) experiments. We have previously shown that the relaxation times of the C^β and C^α deuterons in valine side-chains are much longer than those of methyl deuterons over a wide temperature range and are, thus, saturated in the resulting line shapes within the range of inter-scan delays employed; hence, they do not contribute to the observed signal.[32] Time domain data were left-shifted to the echo maximum and a 500 to 1000 Hz exponential line broadening function was employed. Temperature calibration was carried out by recording the static lead nitrate line shapes.[46]

The ^{2}H quadrupolar CEST measurements for the wt-2f, pS8, and ΔE3 M35-labeled fibrils were performed as described previously[24] using a saturation RF field of 1.3 kHz, off-resonance offsets between −60 and 60 kHz, and a 20 ms saturation time. The detection block consisted of the quadrupolar echo acquisition scheme. For normalization purposes, the profile with a saturation time of 2 μs (as the $t=0$ approximation) was also recorded. The measurements were performed using a 14.1 T NMR spectrometer equipped with a Bruker NEO console and a static wide line low-E probe with a 5 mm diameter coil.[47] The temperature was set to 37 °C. The number of

scans ranged from 256 to 1024, with a larger number used for offsets close to a zero frequency. The inter-scan delay was set to 0.8 s. Spectra were processed with a 0.5 kHz exponential line-broadening function.

The ^2H T_1 (longitudinal relaxation) measurements for the ΔE3 F19-ring-D_5-labeled fibrils were taken using the 9.4 T spectrometer with the inversion recovery sequence for relaxation times below about 200 ms and the saturation recovery sequence for longer times. The multiple-echo (QCPMG) detection scheme was used for signal enhancement[40] without the suppression of relaxation anisotropy.[41] Ten QCPMG echoes were collected with 63 μs pulse spacing. Eight to nine relaxation delays were collected. ^2H QCPMG spectra were processed with 0.2 kHz exponential line broadening.

Modeling

Modeling the line shapes based on the rotameric interconversions (as shown in the models in Figure 2) followed the procedures outlined in detail in prior work.[25,29,31] The EXPRESS program was used.[48] After averaging over the fast methyl jumps, the quadrupolar coupling constant was set to $C_q = 53.3$ kHz for L17, L34, and V36 and 58 kHz for M35, with the asymmetry parameter $\eta = 0$. These values were determined from low temperatures.[31] The fitting parameters of the models, population of the major conformer w, and rotameric exchange rate constant k_{rot} were obtained using the iterative procedure outlined in prior work.[25]

Modeling the longitudinal relaxation rates for the F19 side-chain, detailed in,[27,38] involves the creation of relaxation time libraries to obtain the fits of the central value of the log-normal distribution of the k_{flip} rate constant and the widths of the distribution of the constants σ_k, as shown in Figure S6. The parameters of the small-angle fluctuations around the χ_2 angle (Figure 2D) were fixed, as found for the wt-2f fibrils at $\langle E_a^{small} \rangle = 10.5$ kJ/mol and $\sigma^{small} = 1.7$ kJ/mol, with the single Arrhenius prefactor of $2.17 \cdot 10^{10}$ s^{-1}. The quadrupolar tensor parameter was $C_q = 180$ kHz, $\eta = 0$. The angles between either the C^{δ}–D or the C^{ε}–D bonds and the C^{β}–C^{γ} axis was taken as 59.2°. The amplitude of the small-angle fluctuations in the 4-site jump model of Figure 2D was taken as $\alpha/2 = 5°$. The errors in the fitted model parameters were determined using the inverse covariance matrix method.

The quadrupolar CEST profiles for the M35 side-chain were modeled using the full Liouvillian approach that includes the interconversions of all eight base coherences of spin 1 during the saturation period.[22,24] Longitudinal relaxation was taken into account phenomenologically ($T_1 = 300$ ms) by including an additional term in the Liouvillian evolution matrix. The errors in k_{rot} were determined using the inverse covariance matrix method.

Acknowledgements

This work was supported by a National Institutes of Health Grant 1R15-GM111681. Experiments were performed using a 9.4 T spectrometer at CU Denver supported by NSF grant 1726947. Quadrupolar CEST experiments were performed at the National High Magnetic Field Laboratory, which is supported by NSF Cooperative Agreement NSF/DMR-1644779, the State of Florida, and the U.S. Department of Energy. We thank Dr. Riqiang Fu for technical assistance with these measurements.

Conflict of Interest

The authors declare no conflict of interest.

Keywords: deuterium NMR · solid-state NMR · amyloid-beta fibrils · post-translational modifications · rotameric jumps

[1] J. Hardy, D. J. Selkoe, *Science* **2002**, *297*, 353–356.
[2] E. P. Barykin, V. A. Mitkevich, S. A. Kozin, A. A. Makarov, *Front. Genet.* **2017**, *8*, 58–58.
[3] E. S. Musiek, D. M. Holtzman, *Nat. Neurosci.* **2015**, *18*, 800–806.
[4] J. Rasmussen, J. Mahler, N. Beschorner, S. A. Kaeser, L. M. Hasler, F. Baumann, S. Nystrom, E. Portelius, K. Blennow, T. Lashley, N. C. Fox, D. Sepulveda-Falla, M. Glatzel, A. L. Oblak, B. Ghetti, K. P. R. Nilsson, P. Hammarstrom, M. Staufenbiel, L. C. Walker, M. Jucker, *Proc. Natl. Acad. Sci. USA* **2017**, *114*, 13018–13023.
[5] Y. Xiao, B. Ma, D. McElheny, S. Parthasarathy, F. Long, M. Hoshi, R. Nussinov, Y. Ishii, *Nat. Struct. Mol. Biol.* **2015**, *22*, 499–505.
[6] L. Vugmeyster, D. F. Au, D. Ostrovsky, B. Kierl, R. Fu, Z. W. Hu, W. Qiang, *Biophys. J.* **2019**, *117*, 1524–1535.
[7] A. E. Roher, T. A. Kokjohn, S. G. Clarke, M. R. Sierks, C. L. Maarouf, G. E. Serrano, M. S. Sabbagh, T. G. Beach, *Neurochem. Int.* **2017**, *110*, 1–13.
[8] M. P. Kummer, M. T. Heneka, *Alzheimer's Res. Ther.* **2014**, 6.
[9] S. Kumar, S. Singh, D. Hinze, M. Josten, H.-G. Sahl, M. Siepmann, J. Walter, *J. Biol. Chem.* **2012**, *287*, 8641–8651.
[10] S. Kumar, J. Walter, *Aging* **2011**, *3*, 803–812.
[11] S. Kumar, N. Rezaei-Ghaleh, D. Terwel, D. R. Thal, M. Richard, M. Hoch, J. M. Mc Donald, U. Wullner, K. Glebov, M. T. Heneka, D. M. Walsh, M. Zweckstetter, J. Walter, *EMBO J.* **2011**, *30*, 2255–2265.
[12] A. T. Petkova, W. M. Yau, R. Tycko, *Biochemistry* **2006**, *45*, 498–512.
[13] A. T. Petkova, R. D. Leapman, Z. H. Guo, W. M. Yau, M. P. Mattson, R. Tycko, *Science* **2005**, *307*, 262–265.
[14] Z. W. Hu, L. Vugmeyster, D. F. Au, D. Ostrovsky, Y. Sun, W. Qiang, *Proc. Natl. Acad. Sci. USA* **2019**, *116*, 11253–11258.
[15] Z.-W. Hu, D. F. Au, L. Cruceta, L. Vugmeyster, W. Qiang, *ACS Chem. Neurosci.* **2020**.
[16] Z.-W. Hu, M.-R. Ma, Y.-X. Chen, Y.-F. Zhao, W. Qiang, Y.-M. Li, *J. Biol. Chem.* **2017**, *292*, 2611–2623.
[17] C. J. Pike, M. J. Overman, C. W. Cotman, *J. Biol. Chem.* **1995**, *270*, 23895–23898.
[18] J. Dunys, A. Valverde, F. Checler, *J. Biol. Chem.* **2018**, *293*, 15419–15428.
[19] M. Wulff, M. Baumann, A. Thummler, J. K. Yadav, L. Heinrich, U. Knupfer, D. Schlenzig, A. Schierhorn, J. U. Rahfeld, U. Horn, J. Balbach, H. U. Demuth, M. Fandrich, *Angew. Chem. Int. Ed.* **2016**, *55*, 5081–5084; *Angew. Chem.* **2016**, *128*, 5165–5168.
[20] H. A. Scheidt, J. Adler, M. Krueger, D. Huster, *Sci. Rep.* **2016**, *6*, 33531.
[21] Z. W. Hu, L. Cruceta, S. Zhang, Y. Sun, W. Qiang, *ACS Chem. Neurosci.* **2021**, *12*, 3625–3637.
[22] L. Vugmeyster, *Solid State Nucl. Magn. Reson.* **2021**, *111*, 101710.
[23] L. Vugmeyster, D. Ostrovsky, *Methods* **2018**, *148*, 136–145.
[24] L. Vugmeyster, D. Ostrovsky, R. Fu, *ChemPhysChem* **2020**, *21*, 220–231.
[25] L. Vugmeyster, M. A. Clark, B. I. Falconer, D. Ostrovsky, D. Gantz, W. Qiang, G. L. Hoatson, *J. Biol. Chem.* **2016**, *291*, 18484–18495.
[26] D. F. Au, D. Ostrovsky, R. Fu, L. Vugmeyster, *J. Biol. Chem.* **2019**, *294*, 5840–5853.
[27] L. Vugmeyster, D. Ostrovsky, G. L. Hoatson, W. Qiang, B. I. Falconer, *J. Phys. Chem. B* **2017**, *121*, 7267–7275.
[28] L. Vugmeyster, D. Ostrovsky, M. A. Clark, B. I. Falconer, G. L. Hoatson, W. Qiang, *Biophys. J.* **2016**, *111*, 2135–2148.
[29] L. Vugmeyster, D. Ostrovsky, *J. Biomol. NMR* **2011**, *50*, 119–127.
[30] R. R. Vold, *Nuclear Magnetic Resonance Probes of Molecular Dynamics* (Ed.: R. Tycko), Kluwer academic Publishers, Dordrecht **1994**, pp. 27–112.
[31] L. Vugmeyster, D. Ostrovsky, J. J. Ford, S. D. Burton, A. S. Lipton, G. L. Hoatson, R. L. Vold, *J. Am. Chem. Soc.* **2009**, *131*, 13651–13658.
[32] L. Vugmeyster, D. Ostrovsky, A. Khadjinova, J. Ellden, G. L. Hoatson, R. L. Vold, *Biochemistry* **2011**, *50*, 10637–10646.
[33] Y. Miller, B. Ma, R. Nussinov, *J. Am. Chem. Soc.* **2011**, *133*, 2742–2748.
[34] M. McDonald, H. Box, W. Bian, A. Kendall, R. Tycko, G. Stubbs, *J. Mol. Biol.* **2012**, *423*, 454–461.

[35] A. K. Paravastu, I. Qahwash, R. D. Leapman, S. C. Meredith, R. Tycko, *Proc. Natl. Acad. Sci. USA* **2009**, *106*, 7443–7448.
[36] G. Wagner, A. Demarco, K. Wuthrich, *Biophys. Struct. Mech.* **1976**, *2*, 139–158.
[37] M. Hattori, H. Li, H. Yamada, K. Akasaka, W. Hengstenberg, W. Gronwald, H. R. Kalbitzer, *Protein Sci.* **2004**, *13*, 3104–3114.
[38] L. Vugmeyster, D. Osrovsky, T. R. Villafranca, J. Sharp, W. Xu, A. S. Lipton, G. L. Hoatson, R. L. Vold, *J. Phys. Chem. B.* **2015**, *119*, 14892–14904.
[39] L. Vugmeyster, D. Ostrovsky, *Prog. Nucl. Magn. Reson. Spectrosc.* **2017**, *101*, 1–17.
[40] F. H. Larsen, H. J. Jakobsen, P. D. Ellis, N. C. Nielsen, *Mol. Phys.* **1998**, *95*, 1185–1195.
[41] R. L. Vold, G. L. Hoatson, L. Vugmeyster, D. Ostrovsky, P. J. De Castro, *Phys. Chem. Chem. Phys.* **2009**, *11*, 7008–7012.
[42] R. Morales, I. Moreno-Gonzalez, C. Soto, *PLoS Pathog.* **2013**, *9*, e1003537.
[43] J. R. Harris, J. W. Horne, *Electron Microscopy in Biology* (Ed.: J. R. Harris), Oxford IRL Press **1991**, pp. 203–228.
[44] J. Dubochet, M. Groom, S. Mueller-Neuteboom, *Adv. Opt. Electron Microsc. Vol. 8* (Eds.: R. Barrer, V. E. Cosslett) **1982**, pp. 107–135.
[45] R. L. Vold, R. R. Vold, *Adv. in Magnetic Opt. Reson. Vol. 16* (Ed.: W. Warren), Academic Press, San Diego **1991**, pp. 85–171.
[46] P. A. Beckmann, C. Dybowski, *J. Magn. Reson.* **2000**, *146*, 379–380.
[47] P. L. Gor'kov, E. Y. Chekmenev, C. Li, M. Cotten, J. J. Buffy, N. J. Traaseth, G. Veglia, W. W. Brey, *J. Magn. Reson.* **2007**, *185*, 77–93.
[48] R. L. Vold, G. L. Hoatson, *J. Magn. Reson.* **2009**, *198*, 57–72.

Manuscript received: September 29, 2021
Revised manuscript received: November 10, 2021
Accepted manuscript online: November 26, 2021
Version of record online: December 13, 2021